

Multi-Spectral Optoacoustic Tomography (MSOT) of human breast cancer.

Gael Diot¹, Stephan Metz², Aurelia Noske³, Evangelos Liapis⁴, Barbara Schroeder⁴, Saak V. Ovsepian^{1,4}, Reinhard Meier², Ernst Rummeny², Vasilis Ntziachristos^{1,4}.

¹Chair of Biological Imaging, Technische Universität München, Arcisstraße Str. 1, München 80333, Germany; ²Department of Radiology, Klinikum Rechts der Isar, Technische Universität München, Ismaninger Str. 22, München 81675, Germany; ³Institute of Pathology, Klinikum Rechts der Isar, Technische Universität München, Ismaninger Str. 22, München 81675, Germany; ⁴Institute of Biological and Medical Imaging, Helmholtz Zentrum München, Ingolstädter Landstraße 1, Neuherberg 85764, Germany.

Running title

Spectral signatures of human breast cancer by means of MSOT

Keywords

Photoacoustic; optical imaging; tumors; NIR; handheld; hemoglobin.

Acknowledgements

The research leading to these results has received funding by the Deutsche Forschungsgemeinschaft (DFG), Sonderforschungsbereich-824 (SFB-824), subproject A1 and Gottfried Wilhelm Leibniz Prize 2013 (NT 3/10-1).

Correspondence to:

Vasilis Ntziachristos,
Professor and Chair of Biological Imaging
Technische Universität München.

Address: Institute of Biological and Medical Imaging, Helmholtz Zentrum München, Deutsches Forschungszentrum für Gesundheit und Umwelt (GmbH), Ingolstädter Landstr., 85764 Neuherberg, Germany.

Phone: +49 89 3187 3852

Fax: +49 89 3187 3017

Email: v.ntziachristos@tum.de

Conflict of interest disclosure

Prof. Ntziachristos is stakeholder of iThera Medical GmbH

Other

Word count: 3793

Figures & Tables: 6

Abstract

Purpose:

In a pilot study, we introduce fast handheld Multi-Spectral Optoacoustic Tomography (MSOT) of the breast at 28 wavelengths, aiming to identify high-resolution optoacoustic (photoacoustic) patterns of breast cancer and non-cancerous breast tissue.

Experimental Design:

We imaged 10 female patients aged 48-81 years with malignant non-specific breast cancer or invasive lobular carcinoma. Three healthy volunteers aged 31-36 years were also imaged. Fast-MSOT was based on unique single-frame-per-pulse (SFPP) image acquisition employed to improve the accuracy of spectral differentiation over using a small number of wavelengths. Breast tissue was illuminated at the 700 - 970 nm spectral range over 0.56 seconds total scan time. MSOT data were guided by ultrasonography and X-ray mammography or MRI.

Results:

The extended spectral range allowed the computation of oxygenated hemoglobin (HbO₂), deoxygenated hemoglobin (Hb), total blood volume (TBV), lipid and water contributions, allowing first insights into in-vivo high-resolution breast tissue MSOT cancer patterns. TBV and Hb/HbO₂ images resolved marked differences between cancer and control tissue, manifested as a vessel rich tumor periphery with highly heterogeneous spatial appearance compared to healthy tissue. We observe significant TBV variations between different tumors and between tumors over healthy tissues. Water and fat lipid layers appear disrupted in cancer vs. healthy tissue; however offer weaker contrast compared to TBV images.

Conclusion:

In contrast to optical methods, MSOT resolves physiological cancer features with high resolution and revealed patterns not offered by other radiological modalities. The new features relate to personalized and precision medicine potential.

Statement of translational relevance

Multispectral optoacoustic tomography (MSOT) combines detection of optical contrast with resolution that is much higher than conventional optical imaging methods. In a pilot interrogation using handheld MSOT, we employed 28 wavelengths with frame rates of ~2 Hz to image 3 healthy volunteers and 10 breast cancer patients and identify MSOT imaging features of breast cancer. We show reconstructed images of total blood volume (TBV), oxy-hemoglobin (HbO₂), deoxy-hemoglobin (Hb), lipid and water and observe vascularization and pathophysiological changes in tumors vs. healthy tissue. Initial results point to MSOT as a non-ionizing, label-free method for imaging breast tissue with possible future applications to diagnostics and the assessment of treatment response.

Introduction

Despite advances in diagnosis and therapy, breast cancer remains a leading cause of mortality in women (1). Imaging plays a major role in breast cancer screening, early diagnosis, staging and monitoring the progression of the disease or treatment efficacy. X-ray mammography (XRM) is the most widely used modality for breast cancer detection, despite concerns over the use of ionizing radiation and reduced accuracy in dense breast tissue (2). Ultrasonography (US) is also used as a follow-up modality to differentiate non-malignant cysts from other tumor types (3). Other methods, including MRI and nuclear imaging, have also been employed for breast cancer detection but are not widely employed due to increased cost and low throughput (4). Due to reliance on ionizing radiation, XRM and nuclear imaging methods are not appropriate for frequent imaging sessions, and hence, not suitable for longitudinal assessment of treatment effects. In addition to cost and low throughput limitations, MRI may also require contrast agents for improving detection (5,6), which complicate frequent use. Finally, US suffers from poor contrast and inter-operator variability (7,8). Therefore, despite a wealth of imaging approaches, there has been a constant search for imaging methods that offer complementary information and reduce possible health risks.

Optical imaging has been considered as an alternative to existing radiological methods for breast imaging (9). Diffuse optical spectroscopy (DOS) and tomography (DOT) aimed to resolve pathological alterations of breast tissue by recording oxyhemoglobin (HbO₂), deoxyhemoglobin (Hb), water and lipids (10,11). Hemoglobin images can enable assessment of two key cancer hallmarks: 1. angiogenesis, typically defined as total hemoglobin Hb + HbO₂ or total blood volume (TBV) content in tissue; and 2. hypoxia, computed as the ratio of oxyhemoglobin over total blood volume (12–15). Moreover, it has been recently observed that hemodynamic responses resolved by DOS can identify responders of neoadjuvant chemotherapy (16–19) within a day of treatment. These capacities, along with the low cost of optical instrumentation, the use of non-ionizing energies and the ability to image through several centimeters (>5 cm) of breast tissue, make the optical method attractive for breast cancer imaging. Conversely, the low resolution achieved due to strong scattering compromises image fidelity and quantification and has restricted the widespread clinical application of optical imaging methods.

Optoacoustic imaging is a hybrid imaging modality that resolves optical absorption with resolution that is significantly improved over optical imaging. Resolution improvements lead to better image fidelity and accuracy (20–22). The technique has been considered for breast cancer imaging since the late 1990's (23–25), using different implementations and imaging geometry designs. One design trend has been the use of rigid imaging chambers to contain the target tissue and position the optical illumination and ultrasound components at predetermined positions in relation to the object scanned (23,24,26–31). Typically, the patient lies in the prone position on a bed with the rigid imaging chamber. Alternatively, handheld optoacoustic imaging has been considered for breast cancer imaging, using a linear ultrasound array retrofitted with an illumination source for optoacoustic signal generation (32). Notably, optoacoustic imaging of the breast has used at most two wavelengths, which affords limited information on the spectral content of the breast tissues (28,32,33). While rigid imaging chambers may allow three-dimensional data collection and reconstruction, handheld scanners are more versatile in their use and can operate similarly or simultaneously with US, also applied in handheld mode (32).

We have recently developed a new class of lasers and handheld optoacoustic systems that can perform fast wavelength scanning (20,34). Up to 100 different wavelengths can be scanned each second. Moreover, fast data acquisition hardware can acquire up to 512 channels in parallel, enabling real-time image acquisition. The rich availability of wavelengths can enhance the readings of the optoacoustic method (35). In particular, it has been recently shown that

increasing the number of wavelengths, over previous implementations using 2 wavelengths, can lead to marked improvements in spectral un-mixing accuracy and sensitivity (36). Taking advantage of these developments, we introduce handheld MSOT based on fast-tuning pulsed lasers for multi-spectral imaging of healthy human breast and breast cancer. In a pilot study using 28 wavelengths ranging between 700 and 970 nm and 50Hz pulsing rates, we resolve the distribution of hemoglobin, lipid and water in human volunteers and patients. A primary goal of the study was to identify the patterns achieved by breast MSOT due to the high resolution offered and interrogate possible differences between malignant tumors and between malignant tumors and non-malignant breast tissue. We identify a characteristic disruption of Hb and HbO₂ signals, leading to marked TBV pattern differences between healthy and cancerous breast tissue. We further identify spatial heterogeneity differences between tumors in different patients. We discuss the implications of the findings in terms of designing Phase II clinical trials based on handheld breast cancer MSOT.

Material & Methods

Handheld MSOT

The custom-built handheld MSOT scanner has been previously described (34). In brief, illumination is provided by a tunable pulsed laser (Spitlight 600 DPSS, Innolas Laser, Germany) with working range of 680-980 nm on a per pulse basis and a repetition rate of 50 Hz. Pulse length was 8 ns, and maximum energy at 700 nm was approximately 15 mJ. A custom-made fiber bundle (CeramOptec Germany) delivered light in a line configuration (40 x 1 mm²). Optoacoustic signals were detected using a 256-element piezoelectric transducer array in which the elements were arranged in a half arc spanning 174°. The array diameter was 120 mm, and the central frequency was 5 MHz (see Ref. (34) for a detailed description). The transducer was enclosed in an optically and acoustically transparent low-density polyethylene membrane, with the cavity between the half-arc detector and specimen filled with heavy water (D₂O) for optimal acoustic coupling. The 220-mL D₂O cavity does not come into contact with the patient and requires topping-up (5-10 mL) every few months. A custom-built analog-to-digital 256-channel converter was used for parallel data acquisition at a sampling rate of 40 MS/s and 12-bit digital resolution. To enable real-time viewing of the acquired images, a delay and sum image reconstruction algorithm was implemented on a graphics-processing unit (GPU) that rendered frames at 50 Hz in a graphical interface.

Patients

Ten patients aged 48-81 years that had been diagnosed with malignant, non-specific breast cancer (n = 8) or invasive lobular carcinoma (n = 2) at the Klinikum Rechts der Isar of the Technische Universität München (Munich, Germany) were examined using handheld MSOT. Three of the patients were pre-menopausal, while the remaining seven were menopausal or post-menopausal. All patients were diagnosed initially based on lesions observed by XRM, US and/or MRI, and diagnosis was confirmed based on core needle biopsy. Tumors, which ranged in size from 5 to 50 mm in the long dimension, were classified by an expert radiologist based on the BI-RADS classification scale and immunohistochemistry (HER2, ER and PR) (37). All participants gave written informed consent to participate in the study, which was approved by the Government of Upper Bavaria and by the Ethics Review Board of the Klinikum Rechts der Isar.

Imaging protocol

All patients and healthy controls were scanned by US and MSOT in the supine position. In patients, the masses seen by XRM were located using US (Logiq E9, GE Healthcare, Solingen Germany), and then the same tissue area was scanned using handheld MSOT (Fig. 1a), during which slight pressure was applied to reduce the tumor's depth. A real-time reconstruction algorithm was used to display the resulting images on a graphical user interface (GUI), with raw data stored in parallel for offline post-processing and data analysis. For each MSOT position scanned (cross-sectional slice), 28 frames were collected at wavelengths from 700 to 970 nm in 10-nm steps. Each multi-wavelength slice of 28 frames took ~ 0.56 sec to acquire (i.e. 50 Hz laser pulse repetition rate with a different wavelength for each pulse). The laser pulses triggered the data acquisition (DAQ) module (Fig. 1b). We did not employ data averaging, in order to minimize motion artifacts. Therefore, each single image collected was acquired with a single pulse illumination. Total examination time was 2-4 minutes.

Data analysis and image representation

Data was processed offline with MATLAB R2014b (Mathworks, USA). First, a Butterworth bandpass filter was applied with cut-off frequencies 0.25 MHz and 10 MHz, and signals were corrected for laser energy fluctuations, using an internal photo-sensor that is recording laser output. The sensor was integrated into the laser module, and images obtained at different wavelengths were reconstructed based on a model-based reconstruction algorithm (38). Subsequently, the reconstructed images were linearly un-mixed, using the spectra of the four main endogenous absorbers in the 700-970 nm range (Fig.1c), i.e. oxygenated hemoglobin (HbO₂), deoxygenated hemoglobin (Hb), lipid and water (H₂O), in the 700 to 970 nm spectral range (39). This resulted in four separate images, each corresponding to one of the main absorbers (Fig. 1c). Different colormaps were selected to represent the distributions of the four absorbers: HbO₂, red; Hb, green; lipid, magenta; and H₂O, blue. Image processing calculating image metrics including average values over regions of interest and image profiles employed for assessing spatial heterogeneity were performed on MATLAB (Mathworks, USA). Total blood volume (TBV = Hb + HbO₂) ratios were calculated for 5 x 5 mm² regions of interest from high TBV values on the tumor rim to background tissue, i.e. normal breast tissue away from the tumor. Spatial TBV gradients through tumors were calculated by fitting a line (radius) of 5 mm length to the intensity values across a TBV profile from the center of the tumor to the outer boundary of the tumor and plotting the resulting slope. Similar 5 mm profiles were also drawn in adjacent healthy tissue to obtain reference spatial gradient measurements.

Results

Fig. 2 shows MSOT measurements from a healthy volunteer. Images acquired at different wavelengths reveal different structural information and contrast (Fig. 2a-d). Images at wavelengths in the 700-850 nm range depict a layer of strong signal from the tissue surface (i.e. skin), with an underlying layer of weak optoacoustic signal and then, at lower depth, an area containing several high-resolution structural features attributed to vascular structures. Images at shorter wavelengths (i.e. 750, 850 nm; Fig. 2a, b) showed higher resolution and contrast compared to images at longer wavelengths (i.e. 930 nm; Fig. 2c) reflecting the fact that longer wavelengths are representative of fat and water signals, which reduces contrast in observing hemoglobin. This is in particular evident at >930 nm images (i.e. 970 nm; Fig. 2d), which exhibited a low-spatial variation pattern due to the fact that lipids and water are broadly distributed throughout the breast. Spectral un-mixing applied to all 28 wavelengths produced a set of four images, i.e. HbO₂, Hb, lipid and H₂O (Fig. 2e, g, h). Fig. 2f shows an image of total blood volume, calculated as the sum of HbO₂ and Hb components. A composite image showing the overlap of all four components is depicted in Fig. 2i.

Clearly distinguishable features are present in the different tissue components, pinpointing a stratified organization of the breast tissue, with HbO₂ and Hb revealing vascular-rich tissue areas and vessels (Fig. 2e, f, i), supplying the dermal layer and mammary tissue, while subcutaneous fat and retro-mammary adipose tissue receive sparser vascularization. Anatomically, the information provided by the four components resolved (Fig. 2e-i) is in agreement with the stratified anatomy of the healthy breast (Fig. 2j). The dark subcutaneous layer in panels a, b and d of Fig. 2, more clearly resolved in panel g, likely represents a fat layer because it showed stronger optoacoustic signal at 930 nm (Fig. 2c), near the peak absorption for lipids (Fig. 1c). Future work is needed to verify whether this dark layer corresponds to lipids or to wave reflections or other effects.

Next we used handheld MSOT to image breast cancer. Fig. 3 presents two cases of a 5mm diameter non-specific carcinoma and a 15 x 20-mm diameter invasive lobular carcinoma. The 5mm tumor was a superficial mass with a center at a depth of ~8 mm. The tumor was imaged by MRI after gadolinium injection (Fig. 3a, b) and was visible both by US (Fig. 3c) and MSOT (Fig. 3d). Contrast enhancement with gadolinium shows a “rim-enhancement” effect, corresponding to a tumor that is peripherally perfused but with a core of reduced blood perfusion (Fig. 3b). MSOT resolves a similar pattern of rim-enhancement indicative of strong peripheral vascularization and a core of low optoacoustic signal, observed in Hb-HbO₂ images (Fig. 3e) and total blood volume TBV (i.e. Hb + HbO₂) images (Fig. 3f). Slight but clearly discernible distortion of the lipid and water layers is also evident in the healthy tissue surrounding the breast, possibly due to invasion of the tumor into the adipose tissue and an overall disruption of healthy tissue structures (Fig. 3g, h). Postoperative histology of breast tissue stained with anti-CD31 antibody confirmed the rim enhancement of vascularization (arrows, Fig. 3i), and staining with hematoxylin-eosin identified a dense tumor core (arrow, Fig. 3j).

Fig. 3k-q depict the case of the larger tumor (15 x 20 mm), pathologically characterized as invasive lobular carcinoma ~17 mm under the skin surface. The breast of this patient was denser, as reflected in the high XRM signal from the tissue surrounding the tumor (Fig. 3k), while the tumor itself was clearly visible as a large area of high density (arrow). US also resolved a large solid mass with hypoechoic appearance and ill-defined margins (Fig. 3l), measuring 15 mm along the short and >20 mm along the long dimension. MSOT clearly detected a disruption of the layered structure seen in healthy adipose and fibro-glandular tissue. Fig. 3m-q show MSOT images, which revealed disruption of the normal layered structure of adipose and fibro-glandular tissue. Part of the tumor appeared as a dark area (solid arrow) surrounded by areas of increased but irregular vascularization inside the tumor (total blood volume), with patches of increased hemoglobin signals (Fig. 3m, n and o, hollow arrow), with only one region of the tumor appearing avascular. The avascular tumor region measured approximately 3 mm, smaller than the tumor’s diameter of 15 by 20 mm. No lipid signal was detected inside the tumor (Fig. 3p), while patchy water signals were observed in and around the tumor (Fig. 3q). Postoperative histology of breast tissue stained with anti-CD31 antibody confirmed the presence of a highly vascularized area (hollow arrow Fig. 3r), next to an avascular region (red arrows). H&E staining (Fig 3s) revealed that the avascular area corresponded to a fibro-adenoma (red arrows), next to mammary carcinoma (dotted line + yellow arrows). MSOT allowed in this case to differentiate two types of tumors through their vascularization pattern. The complementarity of contrast between ultrasonography and MSOT is also evident on the images; with US imaging capturing the extent of the entire lesion whereas MSOT only resolving vascularization associated with the malignant part of the tumor.

Fig. 4 shows two additional cases from the largest tumor imaged and deepest seated tumor imaged. Fig.4a shows a non-specific breast carcinoma imaged by XRM and measuring >4cm in the longer diameter. The tumor and surrounding vasculature virtually occupied the

entire MSOT field of view (Fig. 4b-e). The MSOT images demonstrate highly irregular disruption of the layered tissue seen in healthy tissue (Fig. 2). MSOT images showing Hb / HbO₂ (Fig. 4b) and total blood volume (Fig. 4c) revealed irregularities of vascularization and blood distribution, with patches of high HbO₂ throughout the tumor. Superficial and deeper areas of the tissue show patches of increased blood volume, many with high levels of Hb (Fig. 4b). Disruptions of the layered tissue structure were also evident from the spectral maps of lipid (Fig. 4d), which revealed a diffusive signal region (arrow) that may be due to the invading tumor mass. The water signal does not show clear evidence of disruption (Fig. 4e).

A triple negative non-specific carcinoma was imaged at depth of ~ 2.2 cm (tumor extended at depths from ~ 1.7 – 3 cm) Post-gadolinium MRI (Fig. 4f) revealed a circular tumor measuring ~12 mm in diameter, also seen on ultrasound images as a hypoechoic lesion (Fig. 4g). MSOT images (Fig. 4h-k) shows a lesion of increased vascularization with patchy appearance and, as in the previous cases an avascular center appearing dark on the Hb, HbO₂ (Fig. 4h) and TBV images (Fig. 4i). A large feeding vessel appears entering the tumor on the top side of image Fig. 4h and 4i. No significant disruption is seen on the lipid layers (Fig. 4j) and a minor water disruption is seen on the water image (Fig. 4k).

Fig. 5 shows measurements from two additional breast cancer patients and compares images obtained from adjacent planes in the tumor. Fig. 5a presents XRM imaging with iodine-enhanced contrast of a dense breast with a tumor of diameter ~20 mm lying at a depth of 5 mm. The US image of the same area displays a hypoechoic tumor with a highly irregular boundary (Fig. 5b). The corresponding MSOT image (Fig. 5c, e) clearly resolves a tumor mass, exhibiting a patchy rim enhancement indicative of increased blood volume areas. Moreover, a large vessel measuring ~2 mm in diameter seems to reach into the tumor center. Layer disruptions are seen both in the fat and water images. An adjacent MSOT image, obtained ~ 5 mm apart from image Fig. 5e, exhibits a different appearance as it resolves a different part of the tumor mass. A patchy enhancement of total blood volume is observed (Fig. 5d, f), but no central dark area is visible. A layer disruption is seen on both the fat (Fig. 5h) and water layers (Fig. 5j). Images from another patient (Fig. 5k-t) show a breast tumor measuring 25-30 mm in the longer diameter in a second patient. Adjacent MSOT planes 5 mm apart are rendered again to examine differences through different slices through the tumor. Fig. 5k shows the XRM of the breast tumor measuring 25-30 mm in the longer diameter. Irregular, spiculated borders are clearly discernible on the US image (Fig. 5i). MSOT resolves rim enhancement in the total blood volume image, surrounding a dark mass (Fig. 5m, o). Fig. 5q shows the lipid layer, revealing minor disruption, while Fig. 5s shows the water layer, which indicated no apparent tumor-induced changes. In the second imaging plane (Fig. 5-n, p), Hb/HbO₂ and total blood volume MSOT images revealed features different from those in the first imaging plane, including different patches of high Hb signal as well as strong HbO₂ signal around a dark avascular core. This suggests increased angiogenesis of areas surrounding an apparent weaker signal mass lying deeper than in the first imaging plane (arrow). US confirmed hypoechoic areas that extended deeper than the main mass (arrow on Fig. 5l), which is clearly seen on the MSOT images (arrow on Fig. 5n). This secondary dark-center mass (Fig. 5n and p, arrow) shows rich lipid content (Fig. 5r), which was unusual among the lesions analyzed in this study. Overall, this secondary lesion also appears to impart a disruption of the deeper fat layer (Fig. 5r), but not prominently in the water layer (Fig. 5t).

To better understand the manifestation of the MSOT features resolved in breast cancer we computed 2 parameters based on the imaging feature observed, i.e. the TBV tumor to background ratio (Fig. 6a) and the TBV gradient (Fig. 6b). The first parameter computed the ratio of the total blood volume (TBV = Hb + HbO₂) seen in highly vascular areas of tumors vs. background normal tissue over a 5x5 mm² ROI. The TBV ratio indicates the relative

angiogenesis in tumors and reached values as high as 30-fold (Fig. 6a). The ratio in tumor #3 is computed for the patient shown on Fig.4a-e. Due to the large area occupied by the tumor, it is not likely in this case that normal tissue is present on the image; therefore, the value may not represent an accurate tumor to background ratio. The findings demonstrate that in all cases there is a marked increase in TBV signal in cancerous tumors, indicative of angiogenesis. Nevertheless, the findings also demonstrated significant variability between tumors, allowing observations on the individual tumor level. Due to the presence of high resolution images, intra-tumoral variability could also be observed. To capture aspects of tumor heterogeneity we also applied the TBV gradient as a metric of tumor spatial heterogeneity. The TBV gradient (Fig. 6b) was calculated as the angle of a 5mm line profile (radius) applied to tumors and adjacent non-cancerous tissue. The TBV gradient indicates spatial heterogeneity from the periphery to the center of the tumor and similarly exhibited more than 5-fold variability for different tumors imaged. The strongest gradient value is in the case of patient #4, which was a triple negative stage 3 tumor, followed closely by patient #7, which was a double negative (PR-, HER2-) patient. Fig. 6c shows a summary of the immunohistochemical readings for estrogen receptors (ER), progesterone receptors (PR) and tyrosine-protein kinase receptor (HER 2) for all patients. The age, sex and tumor grading and type are also specified.

Discussion

We performed a pilot imaging study aimed to identify MSOT patterns in healthy breast tissue and breast cancer, resolved in label free mode. Handheld MSOT is emerging in clinical applications; however, it has never been previously applied to breast cancer studies. Observation of breast MSOT patterns revealed recurring features including high peripheral vascularization, increased TBV heterogeneity over normal tissue, low intra-tumoral vascularity, disruption of tissue layers such as fat and water layers, and patchy appearance of HB and HBO₂ signals.

High-peripheral vascularity was visualized on Hb, HbO₂ and TBV images, which demonstrated areas of increased TBV indicative of angiogenesis, a hallmark of cancer development (40–43). Compared to healthy breast tissue, tumor areas exhibited a strong heterogeneous TBV pattern with markedly reduced vascularization in the tumor core. High resolution MSOT patterns of angiogenesis and tumor vascular heterogeneity were captured by the TBV ratio and the TBV gradient calculations respectively (Fig. 6). Regions of interest from the tumor periphery (rim) vs. adjacent non-cancerous tissue demonstrated Target to Background Ratios (TBR) that could reach values of > 30-fold increase (Tumor #7, #8; Fig. 6a).

CD31 immunohistochemistry analysis on surgically excised specimen (e.g. Fig. 3i, 3r) confirmed patches of high vasculature surrounding the tumor. The reduced optoacoustic signal (dark area) observed in the core of tumors is explained herein as low intra-tumoral vascularization. Histopathology analysis of the tumor core, available for a subset of tumors that did not receive neoadjuvant chemotherapy (Fig. 3i, j) revealed vessels with size that would generate high ultrasound frequencies (>7 Mhz), which are not detected by the ultrasound transducer employed. It is unlikely that this lack of signal is due to light blockage because of increased photon absorption by the increased vascularization, since there are no “shadowing” effects observed by the tumor. Moreover, Fig. 5a clearly resolves a large blood vessel reaching the tumor center, corroborating the hypothesis that light reaches the tumor core. Tumors also exhibited marked spatial heterogeneity of vascular features, with normalized gradient differences ranging from 0.2 to 1 (Fig. 6b) and the TBV gradient assuming the highest values for the two PR- negative patients in the study (patient #4, #7).

MSOT also allowed the observation of the individual HbO₂ and Hb images contributing to TBV and consistently demonstrated patches of increased HbO₂ content in the tumor periphery. Some tumors were shown to contain strong deoxygenated hemoglobin signals, indicative of settling hypoxia into the tumor mass. However, this observation was not present in all tumors, possibly pointing to a variation in hypoxia between tumors. MSOT also resolved an apparent disruption of the lipid and water layered structures observed in healthy breast. The disruption was seen on all images, however its strength varied significantly and did not preliminary evinced on an MSOT pattern with diagnostic potential, since not all tumors could be clearly identified on the fat or water images. Imaging of large tumors in Fig. 4 and Fig. 5q showed strong lipid infiltration in the tumor area, whereby imaging of smaller tumors, such as in Fig. 3, did not show colocalization of the tumor mass and fat signals.

MSOT images demonstrated different patterns compared to the appearance of the tumors on ultrasonography. The dense vascular patterns observed, indicating malignancy (42,44), could play a role in tumor characterization within the BIRADS classification or for cartography of intra-tumoral heterogeneity leading to improved biopsy guidance. This possibility was exemplified in Fig. 3l and Fig. 6n, whereby ultrasound identified a large mass containing fibro adenoma and malignant tumor, whereby MSOT detected the highly vascular malignant lesion. In a second example, Fig. 3c, f depict markedly different tumor appearance between MSOT and ultrasound images, with MSOT exhibiting a highly heterogeneous pattern extending well beyond the lesion seen by ultrasonography. Such complementary contrast between MSOT and ultrasonography may change the views on tumor mass extent and biopsy guidance.

MSOT may be further clinically useful for identifying tumor skin infiltration. Disruptions of the melanin layer and skin vascularization, seen on Fig. 4, could guide surgery and overall therapy planning when skin infiltration is suspected. MSOT could help avoiding punch biopsies, especially since current mammographic imaging cannot distinguish between cutaneous edema (e.g. due to lymph node metastasis) and tumor skin infiltration. Furthermore, the extent of the tumor to subcutaneous layers is valuable in planning subcutaneous mastectomy.

Compared to diffuse optical imaging (DOI) of breast cancer (10–19,45–49), the MSOT patterns found showcase the merits of the superior optoacoustic resolution. DOI cannot observe vascularization patterns, due to the strong photon scattering in tissue and the low resolution achieved. In contrast to optoacoustic methods which resolve breast tumors with 200-300 micrometer resolution, DOI methods offer resolution of 2-3 mm or lower. Therefore, only a bulk value per tumor mass can be typically recorded. Moreover, photon diffusion leads to an imaging problem that is highly ill-posed, a feature which significantly reduces the quantification accuracy over high-resolution methods and may lead to strong image artifacts. Therefore, DOI has not been shown suitable to observe the morphological tumor characteristics observed by MSOT.

The MSOT system described here offers novel features compared to previous optoacoustic studies employing at most 2 wavelengths (25,36). Advanced illumination and detection technology enabled MSOT at 28 wavelengths at ~2 Hz scan times. The use of a large number of wavelengths improves the accuracy of spectral unmixing over systems using 2 wavelengths [41] and enabled unmixing of four spectral components. In addition, fast scanning technology minimizes motion artifacts, which allows seamless co-registration of images collected at different wavelengths and improves the accuracy of spectral unmixing. The MSOT implementation herein also employed curved arrays for improving resolution and overall image

quality (32) over linear ultrasound element-arrays or fixed scan geometries that yield lower resolution (25). Conversely, handheld systems are more sensitive to motion over fixed geometries. Moreover, access to deep seated tumors may require adjustment of the handheld scanner in order to obtain a preferable angle of access, in analogy to practices common in handheld ultrasonography.

Despite the recent technical advances described in the previous paragraph, handheld MSOT can be substantially improved. One advance would be to integrate US into the handheld device, in order to allow truly multimodal imaging allowing for accurate image registration between the two modalities, in analogy to implementations developed in small animal imaging (50). Another improvement would be to reduce the effects of wavelength- and depth-dependent fluence attenuation on the optoacoustic images (36). This would be particularly important for accurately calculating oxygen saturation (SO₂) maps, especially since it has been shown that SO₂ images based on linear unmixing become inaccurate with increasing depth (36). It may also be useful to include absorption of melanin in MSOT unmixing, in order to improve imaging of skin oxygenation.

Overall, MSOT allowed individualized label-free readings of vascularization/angiogenesis patterns in high-resolution, enabling understanding of parameters not only on a per tumor level but even within the intra-tumoral environment, revealing variations in the tumor spatial heterogeneity amongst tumors. High peripheral TBV values and weak intra-tumoral TBV contributions were preliminary shown to differentiate tumors from adjacent non-malignant tissues in a broad range of tumor sizes; nevertheless achieving highest TBV contrast in smaller tumors. Understanding this spatial tumor heterogeneity may provide valuable insights into breast cancer pathogenesis, progression, and response to treatment. Some tumors exhibited strong Hb signals, indicative of tumor hypoxia. In the future, careful analysis of Hb and inferred tissue hypoxia may be useful in assessing functional aspects of tumors. Moreover, oxygenated hemoglobin, HbO₂, flare has been suggested as an early predictor of neo-adjuvant chemotherapy (46). High-resolution HbO₂ imaging afforded by MSOT may lead to more precise localization of these signals in relation to the tumors, possibly improving the overall accuracy of the observation. In the future, we expect improvements in the quantification of spectral components, especially in regard to correcting for the effects of depth- and wavelength-dependent fluence effects on the data collected (36) and relation of the patterns observed to diagnostic and theranostic applications.

Acknowledgements

The research leading to these results has received funding by the Deutsche Forschungsgemeinschaft (DFG), Sonderforschungsbereich-824 (SFB-824), subproject A1 and Gottfried Wilhelm Leibniz Prize 2013 (NT 3/10-1).

References

1. Torre LA, Bray F, Siegel RL, Ferlay J, Lortet-Tieulent J, Jemal A. Global cancer statistics, 2012. *CA Cancer J Clin* [Internet]. 2015;65:87–108. Available from: <http://dx.doi.org/10.3322/caac.21262>
2. Cardoso F, Harbeck N, Fallowfield L, Kyriakides S, Senkus E, Group on behalf of the EGW. Locally recurrent or metastatic breast cancer: ESMO Clinical Practice Guidelines for diagnosis, treatment and follow-up. *Ann Oncol* [Internet]. 2012;23:vii11-vii19. Available from: http://annonc.oxfordjournals.org/content/23/suppl_7/vii11.short
3. Sickles EA. Breast Imaging: From 1965 to the Present. *Radiology* [Internet]. 2000;215:1–16. Available from: <http://pubs.rsna.org/doi/abs/10.1148/radiology.215.1.r00ap151>
4. Saslow D, Boetes C, Burke W, Harms S, Leach MO, Lehman CD, et al. American Cancer Society Guidelines for Breast Screening with MRI as an Adjunct to Mammography. *CA Cancer J Clin* [Internet]. John Wiley & Sons, Ltd.; 2007;57:75–89. Available from: <http://dx.doi.org/10.3322/canjclin.57.2.75>
5. Kriege M, Brekelmans CTM, Boetes C, Besnard PE, Zonderland HM, Obdeijn IM, et al. Efficacy of MRI and Mammography for Breast-Cancer Screening in Women with a Familial or Genetic Predisposition. *N Engl J Med* [Internet]. 2004;351:427–37. Available from: <http://www.nejm.org/doi/full/10.1056/NEJMoa031759>
6. Turnbull L, Brown S, Harvey I, Olivier C, Drew P, Napp V, et al. Comparative effectiveness of MRI in breast cancer (COMICE) trial: a randomised controlled trial. *Lancet* [Internet]. 375:563–71. Available from: <http://www.sciencedirect.com/science/article/pii/S0140673609620705>
7. Teh W, Wilson ARM. The role of ultrasound in breast cancer screening. A consensus statement by the European Group for breast cancer screening. *Eur J Cancer* [Internet]. 1998;34:449–50. Available from: <http://www.sciencedirect.com/science/article/pii/S0959804997100661>
8. Berg WA, Gutierrez L, NessAiver MS, Carter WB, Bhargavan M, Lewis RS, et al. Diagnostic Accuracy of Mammography, Clinical Examination, US, and MR Imaging in Preoperative Assessment of Breast Cancer. *Radiology* [Internet]. 2004;233:830–49. Available from: <http://pubs.rsna.org/doi/abs/10.1148/radiol.2333031484>
9. Ntziachristos V, Yodh AG, Schnall M, Chance B. Concurrent MRI and diffuse optical tomography of breast after indocyanine green enhancement. *Proc Natl Acad Sci* [Internet]. 2000;97:2767–72. Available from: <http://www.pnas.org/content/97/6/2767.abstract>
10. Grosenick D, Rinneberg H, Cubeddu R, Taroni P. Review of optical breast imaging and spectroscopy. *J Biomed Opt* [Internet]. 2016;21:91311. Available from: <http://dx.doi.org/10.1117/1.JBO.21.9.091311>
11. Fang Q, Selb J, Carp S A S, Boverman G, Miller EL, Brooks DH, et al. Combined optical and X-ray tomosynthesis breast imaging. *Radiology* [Internet]. 2011;258:89–97. Available from: <http://radiology.rsna.org/content/258/1/89.short%5Cnhttp://www.pubmedcentral.nih.gov/articlerender.fcgi?artid=3009384&tool=pmcentrez&rendertype=abstract>
12. Brown JQ, Wilke LG, Geradts J, Kennedy SA, Palmer GM, Ramanujam N. Quantitative optical spectroscopy: A robust tool for direct measurement of breast cancer vascular oxygenation and total hemoglobin content in vivo. *Cancer Res* [Internet]. 2009;69:2919–26. Available from: <http://www.ncbi.nlm.nih.gov/pmc/articles/PMC2677720/>
13. Tromberg BJ, Pogue BW, Paulsen KD, Yodh AG, Boas DA, Cerussi AE. Assessing the future of diffuse optical imaging technologies for breast cancer management. *Med Phys*. 2008;35:2443–51.

14. Leproux A, Kim YM, Min JW, McLaren CE, Chen W-P, O'Sullivan TD, et al. Differential diagnosis of breast masses in South Korean premenopausal women using diffuse optical spectroscopic imaging. *J Biomed Opt.* 2016;21:74001.
15. Wang J, Jiang S, Li Z, diFlorio-Alexander RM, Barth RJ, Kaufman PA, et al. In vivo quantitative imaging of normal and cancerous breast tissue using broadband diffuse optical tomography. *Med Phys* [Internet]. 2010;37:3715–24. Available from: <http://scitation.aip.org/content/aapm/journal/medphys/37/7/10.1118/1.3455702>
16. Jiang S, Pogue BW, Carpenter CM, Poplack SP, Wells WA, Kogel CA, et al. Evaluation of Breast Tumor Response to Neoadjuvant Chemotherapy with Tomographic Diffuse Optical Spectroscopy: Case Studies of Tumor Region-of-Interest Changes. *Radiology* [Internet]. 2009;252:551–60. Available from: <http://pubs.rsna.org/doi/abs/10.1148/radiol.2522081202>
17. Tromberg BJ, Zhang Z, Leproux A, O'Sullivan TD, Cerussi AE, Carpenter PM, et al. Predicting Responses to Neoadjuvant Chemotherapy in Breast Cancer: ACRIN 6691 Trial of Diffuse Optical Spectroscopic Imaging. *Cancer Res.* 2016;76:5933–44.
18. Choe R, Corlu A, Lee K, Durduran T, Konecky SD, Grosicka-Koptyra M, et al. Diffuse optical tomography of breast cancer during neoadjuvant chemotherapy: A case study with comparison to MRI. *Med Phys* [Internet]. 2005;32:1128–39. Available from: <http://doi.wiley.com/10.1118/1.1869612>
19. Pakalniskis M, Wells W. Tumor angiogenesis change estimated by using diffuse optical spectroscopic tomography: demonstrated correlation in women undergoing neoadjuvant chemotherapy for invasive breast cancer? *Radiology* [Internet]. 2011;259:365–74. Available from: <http://radiology.rsna.org/content/259/2/365.short>
20. Taruttis A, Ntziachristos V. Advances in real-time multispectral optoacoustic imaging and its applications. *Nat Phot* [Internet]. Nature Publishing Group, a division of Macmillan Publishers Limited. All Rights Reserved.; 2015;9:219–27. Available from: <http://dx.doi.org/10.1038/nphoton.2015.29>
21. Ntziachristos V. Going deeper than microscopy: the optical imaging frontier in biology. *Nat Meth* [Internet]. Nature Publishing Group, a division of Macmillan Publishers Limited. All Rights Reserved.; 2010;7:603–14. Available from: <http://dx.doi.org/10.1038/nmeth.1483>
22. Wang L V, Yao J. A practical guide to photoacoustic tomography in the life sciences. *Nat Meth* [Internet]. Nature Publishing Group, a division of Macmillan Publishers Limited. All Rights Reserved.; 2016;13:627–38. Available from: <http://dx.doi.org/10.1038/nmeth.3925>
23. Ermilov SA, Fronheiser MP, Nadvoretzky V, Brecht H-P, Su R, Conjusteau A, et al. Real-time optoacoustic imaging of breast cancer using an interleaved two laser imaging system coregistered with ultrasound. *Bios.* International Society for Optics and Photonics; 2010. page 75641W–75641W–7.
24. Kruger RA, Kuzmiak CM, Lam RB, Reinecke DR, Del Rio SP, Steed D. Dedicated 3D photoacoustic breast imaging. *Med Phys* [Internet]. 2013;40:113301. Available from: <http://scitation.aip.org/content/aapm/journal/medphys/40/11/10.1118/1.4824317>
25. Heijblom M, Piras D, van den Engh FM, van der Schaaf M, Klaase JM, Steenbergen W, et al. The state of the art in breast imaging using the Twente Photoacoustic Mammoscope: results from 31 measurements on malignancies. *Eur Radiol* [Internet]. 2016;1–14. Available from: <http://dx.doi.org/10.1007/s00330-016-4240-7>
26. Menke J. Photoacoustic breast tomography prototypes with reported human applications. *Eur Radiol* [Internet]. 2015;25:2205–13. Available from: <http://dx.doi.org/10.1007/s00330-015-3647-x>

27. Heijblom M, Piras D, Brinkhuis M, van Hespden JCG, van den Engh FM, van der Schaaf M, et al. Photoacoustic image patterns of breast carcinoma and comparisons with Magnetic Resonance Imaging and vascular stained histopathology. *Sci Rep* [Internet]. The Author(s); 2015;5:11778. Available from: <http://dx.doi.org/10.1038/srep11778>
28. Fukutani K, Someda Y, Taku M, Asao Y, Kobayashi S, Yagi T, et al. Characterization of photoacoustic tomography system with dual illumination. 2011. page 78992J–78992J–7. Available from: <http://dx.doi.org/10.1117/12.873690>
29. Ermilov SA, Fronheiser MP, Brecht H-P, Su R, Conjusteau A, Mehta K, et al. Development of laser optoacoustic and ultrasonic imaging system for breast cancer utilizing handheld array probes. *SPIE BiOS Biomed Opt. International Society for Optics and Photonics*; 2009. page 717703–10.
30. Kruger RA, Lam RB, Reinecke DR, Del Rio SP, Doyle RP. Photoacoustic angiography of the breast. *Med Phys* [Internet]. American Association of Physicists in Medicine; 2010;37:6096–100. Available from: <http://dx.doi.org/10.1118/1.3497677>
31. Oraevsky AA, Savateeva E V, Solomatin S V, Karabutov AA, Gatalica Z, Khamapirad T. Diagnostic imaging of breast cancer microvasculature with optoacoustic tomography. *Eng Med Biol 2002 24th Annu Conf Annu Fall Meet Biomed Eng Soc EMBS/BMES Conf 2002 Proc Second Jt. IEEE*; 2002. page 2329–30.
32. Ermilov S, Stein A, Conjusteau A, Gharieb R, Lacewell R, Miller T, et al. Detection and noninvasive diagnostics of breast cancer with 2-color laser optoacoustic imaging system. 2007. page 643703–11. Available from: <http://dx.doi.org/10.1117/12.714039>
33. Neuschmelting V, Burton NC, Lockau H, Urich A, Harmsen S, Ntziachristos V, et al. Performance of a Multispectral Optoacoustic Tomography (MSOT) System equipped with 2D vs. 3D Handheld Probes for Potential Clinical Translation. *Photoacoustics* [Internet]. Elsevier; 2016;4:1–10. Available from: <http://www.ncbi.nlm.nih.gov/pmc/articles/PMC4811917/>
34. Buehler A, Kacprowicz M, Taruttis A, Ntziachristos V. Real-time handheld multispectral optoacoustic imaging. *Opt Lett* [Internet]. OSA; 2013;38:1404–6. Available from: <http://ol.osa.org/abstract.cfm?URI=ol-38-9-1404>
35. Taruttis A, van Dam GM, Ntziachristos V. Mesoscopic and Macroscopic Optoacoustic Imaging of Cancer. *Cancer Res.* 2015;
36. Tzoumas S, Nunes A, Olefir I, Stangl S, Symvoulidis P, Glasl S, et al. Eigenspectra optoacoustic tomography achieves quantitative blood oxygenation imaging deep in tissues. *Nat Commun* [Internet]. Nature Publishing Group; 2016;7:12121. Available from: <http://www.ncbi.nlm.nih.gov/pmc/articles/PMC4931322/>
37. D’Orsi CJ, Sickles EA, Mendelson EB, Morris EA. *ACR BI-RADS® Atlas, Breast Imaging Reporting and Data System*. Reston, VA: American College of Radiology; 2013.
38. Rosenthal A, Razansky D, Ntziachristos V. Fast semi-analytical model-based acoustic inversion for quantitative optoacoustic tomography. *IEEE Trans Med Imaging.* 2010;29:1275–85.
39. Pahl S. Tabulated molar extinction coefficient for hemoglobin in water. *Oregon Med Laser Cent.* 1998;4.
40. Holash J, Maisonpierre PC, Compton D, Boland P, Alexander CR, Zagzag D, et al. Vessel Cooption, Regression, and Growth in Tumors Mediated by Angiopoietins and VEGF. *Science* (80-). 1999;284:1994–8.
41. Yancopoulos GD, Davis S, Gale NW, Rudge JS, Wiegand SJ, Holash J. Vascular-specific growth

- factors and blood vessel formation. *Nature* [Internet]. Macmillan Magazines Ltd.; 2000;407:242–8. Available from: <http://dx.doi.org/10.1038/35025215>
42. Hanahan D, Weinberg RA. Hallmarks of Cancer: The Next Generation. *Cell* [Internet]. Elsevier; 144:646–74. Available from: <http://dx.doi.org/10.1016/j.cell.2011.02.013>
 43. Gatenby RA, Gillies RJ. Why do cancers have high aerobic glycolysis? *Nat Rev Cancer* [Internet]. Nature Publishing Group; 2004;4:891–9. Available from: <http://dx.doi.org/10.1038/nrc1478>
 44. Nishida N, Yano H, Nishida T, Kamura T, Kojiro M. Angiogenesis in cancer. *Vasc Health Risk Manag*. 2006;2:213–9.
 45. Ueda S, Roblyer D, Cerussi A, Durkin A, Leproux A, Santoro Y, et al. Baseline tumor oxygen saturation correlates with a pathologic complete response in breast cancer patients undergoing neoadjuvant chemotherapy. *Cancer Res*. 2012;72:4318–28.
 46. Roblyer D, Ueda S, Cerussi A, Tanamai W, Durkin A, Mehta R, et al. Optical imaging of breast cancer oxyhemoglobin flare correlates with neoadjuvant chemotherapy response one day after starting treatment. *Proc Natl Acad Sci* [Internet]. 2011;108:14626–31. Available from: <http://www.pnas.org/cgi/doi/10.1073/pnas.1013103108>
 47. Cerussi A, Hsiang D, Shah N, Mehta R, Durkin A, Butler J, et al. Predicting response to breast cancer neoadjuvant chemotherapy using diffuse optical spectroscopy. *Proc Natl Acad Sci U S A* [Internet]. National Academy of Sciences; 2007 [cited 2017 Jun 21];104:4014–9. Available from: <http://www.ncbi.nlm.nih.gov/pubmed/17360469>
 48. Jiang S, Pogue BW, Kaufman PA, Gui J, Jermyn M, Frazee TE, et al. Predicting breast tumor response to neoadjuvant chemotherapy with Diffuse Optical Spectroscopic Tomography prior to treatment. *Clin Cancer Res*. 2014;20.
 49. Jiang S, Pogue BW. A Comparison of Near-Infrared Diffuse Optical Imaging and 18F-FDG PET/CT for the Early Prediction of Breast Cancer Response to Neoadjuvant Chemotherapy. *J Nucl Med* [Internet]. 2016;57:1166–7. Available from: <http://jnm.snmjournals.org/cgi/doi/10.2967/jnumed.116.174367>
 50. Olefir I, Merčep E, Burton NC, Ovsepian S V, Ntziachristos V. Hybrid multispectral optoacoustic and ultrasound tomography for morphological and physiological brain imaging. *J Biomed Opt* [Internet]. 2016;21:86005. Available from: <http://dx.doi.org/10.1117/1.JBO.21.8.086005>

Figure 1. (a) Photograph of the handheld MSOT probe and a schematic of MSOT scanning breast tissue. (b) Hardware components employed in image acquisition and generation of a multi-spectral dataset at 28 wavelengths. HS – handheld scanner; DAQ – data acquisition unit; OPO – optical parametric oscillator; PC – personal computer. (c) Normalized absorptivity graph of four key absorbers in the breast tissue in the range of wavelengths used. Based on defined spectra, distributions of the four different components (HbO₂, Hb, lipid and H₂O) were extracted from the 28 acquired frames and assigned a different color.

Figure 2. MSOT images of healthy breast tissue revealing spectral and structural information from four endogenous absorbers. (a - d) Raw images acquired at four different wavelengths. (e) Image of HbO₂ and Hb distribution after unmixing of the raw images (a-d), (f) Image of total blood volume distribution. (g, h) Lipid and H₂O components after unmixing as in panels e-f. (i) Composite image of all four absorbers, revealing the layered structure of the breast. (j) Schematic of the structure and layers of the human breast: yellow - skin; pink - lipid; light blue - mammary tissue; green - connective tissue known as Cooper's ligament. Scale bars - 5 mm.

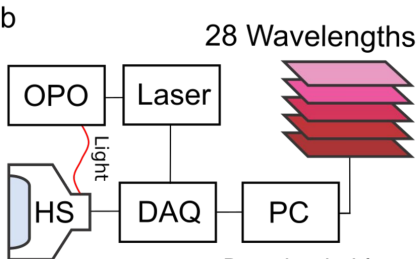
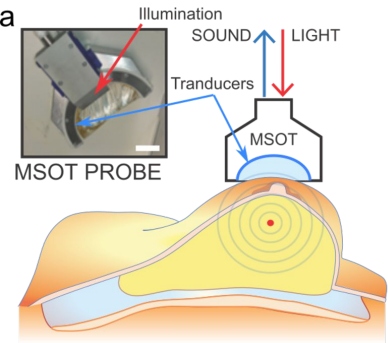
Figure 3. Multimodal imaging of non-specific cancer and invasive lobular carcinoma (a) Axial post-gadolinium MRI showing a 5-mm diameter non-specific breast tumor located at ~8mm depth. The tumor location is indicated with an orange arrow. (b) Enlarged image of the boxed area in panel a. The arrow indicates the tumor body. Higher gadolinium intake (contrast) is visible on the periphery of the tumor, while the tumor core appears darker, suggestive of reduced perfusion. (c) US image of the same tumor providing complementary structural information. (d) Composite MSOT image of the same tumor showing all four key absorbers after un-mixing. (e) MSOT image color-coding the distributions of Hb and HbO₂. (f) MSOT image of total blood volume (TBV). (g) MSOT image of fat content. (h) MSOT image of water content. (i) Anti-CD31 immunohistochemical staining of a cross-sectional slice through the tumor obtained postoperatively. (j) H&E staining of a slice adjacent to the one in panel i. Scale bars (a - h), 5 mm. Scale bars (i - j), 2 mm. – (k) XRM image from a second patient shown a 15 mm x 20mm invasive lobular breast carcinoma indicated by a solid orange arrow. (l) US image revealing a center at location of ~ 17mm deep. (m) Composite MSOT image, indicating a strong disruption of the layered structure of the tissue around the tumor. (n) MSOT image of hemoglobin (Hb and HbO₂) map. (o) MSOT image of total blood volume. (p) MSOT image of lipid. (q) MSOT image of water. (r) Anti-CD31 immunohistochemical staining of a cross-sectional slice through the tumor obtained postoperatively. (s) H&E staining of a slice adjacent to the one in panel r. Scale bars (k - q), 5 mm. Scale bars (r - s), 2 mm.

Figure 4. Multimodal imaging the largest and the deepest seated tumor in the study. (a) XRM image revealing a >4 cm, subcutaneous, non-specific breast tumor by XRM and MSOT. The field of view imaged by MSOT is approximately indicated by a dashed-line box (b) MSOT image of Hb and HbO₂ obtained from the box in (a); arrows point to areas of increased blood volume (c) MSOT image of total blood volume showing constitutive hyperemia through an extended area of the tumor (d) MSOT image of lipid showing disruption of the fat layer (arrow) at the area of the tumor mass. (e) MSOT image of water. (f) Axial MRI breast image after gadolinium injection from a second patient with a triple negative ~12 mm-diameter non-specific tumor (g) US image of the same tumor resolving the tumor at a depth of ~22 mm. (h) Hb, HbO₂ MSOT map (i) Total blood volume revealing patches of increased intensity surrounding the tumor. A large blood vessel appears to infiltrate the tumor. As in previous cases, the core of the tumor appears avascular. (j) Lipid map and (k) H₂O map showing disruptions in the tumor area. Scale bars on MSOT images: 5 mm.

Figure 5. Individualized tumor heterogeneity revealed by MSOT analyzed in two additional patients. (a) Iodine-enhanced XRM of a breast tumor showing a non-specific carcinoma measuring 13mm in diameter. (b) US image of the same tumor. (c) Cross-sectional Hb-HbO₂ image through the

tumor (d) an adjacent cross-sectional Hb-HbO₂ image through the tumor, obtained 5mm apart from the section in (c), exhibiting a different pattern of angiogenesis (e, f) Total blood volume maps corresponding to c, d. The panel (e) depicts a large vessel entering the core of the tumor and an overall reduced TBV value at the tumor core. (g, h) Corresponding lipid cross-sections showing disruption of the retro-mammary layer with lipid invasion into the tumor core. (i, j) MSOT cross-sectional images of the H₂O component showing local disruption of the water content. (k, l) XRM and US images of an irregularly shaped tumor with diameter 2.5-3 cm. (m, n) Adjacent Hb-HbO₂ maps 5mm apart showing high density of small vessels at the edges of the tumor. (o, p) Corresponding TBV images exhibiting differences of angiogenesis patterns through the tumor. (q, r) Lipid maps and (s, t) H₂O maps showing disruption of the lipid layer and reduced H₂O in the tumor-affected area.

Figure 6. Quantification of tumor parameters compared to healthy tissue. (a) Ratio of the TBV intensity in tumors compared to healthy tissue. Healthy tissue is set as the reference at value 1. We note that the TBV ratio calculation for patient #3 may not be representative of true tumor to background ratio since the tumor was very extended spatially (See Fig. 3) and the entire field of view of the MSOT image may have not contained truly healthy tissue. (b) Intensity gradient across tumor compared to healthy tissue. (c) Table containing the immunohistochemistry (ER – PR – HER 2) results, the age, the type of tumor and the stage of all the scanned patients.



Downloaded from clincancerres.aacrjournals.org on September 11, 2015. Copyright © 2015 American Association for Cancer Research.

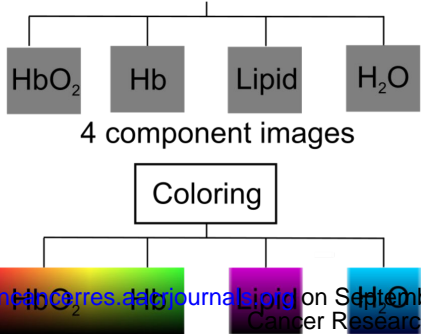
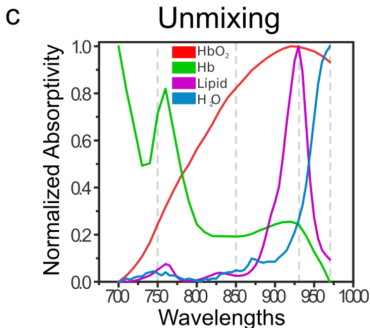
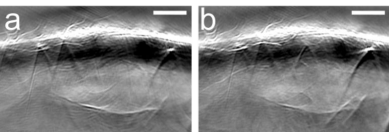
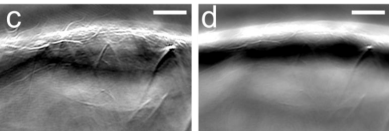


Figure 2



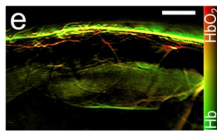
750 nm

850 nm

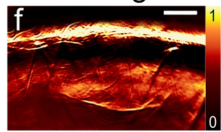


930 nm

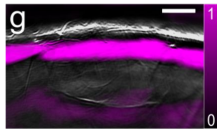
970 nm



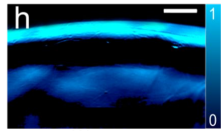
Hb - HbO₂ Map



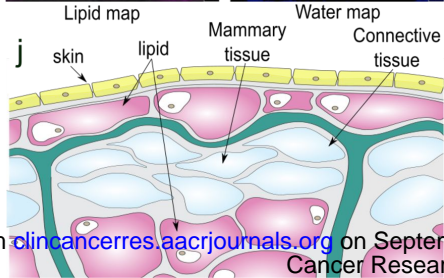
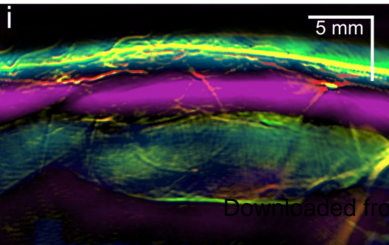
Total blood volume

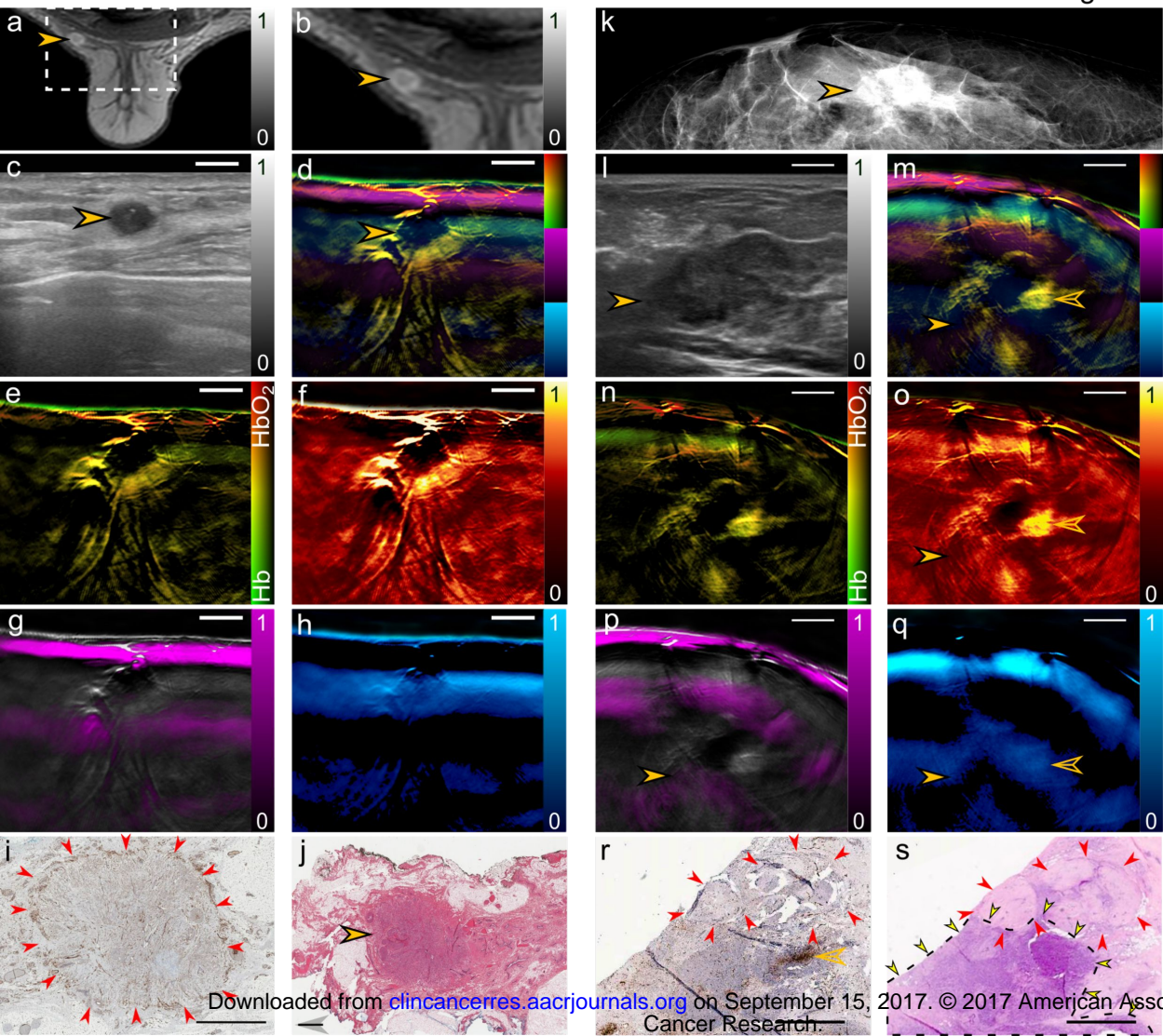


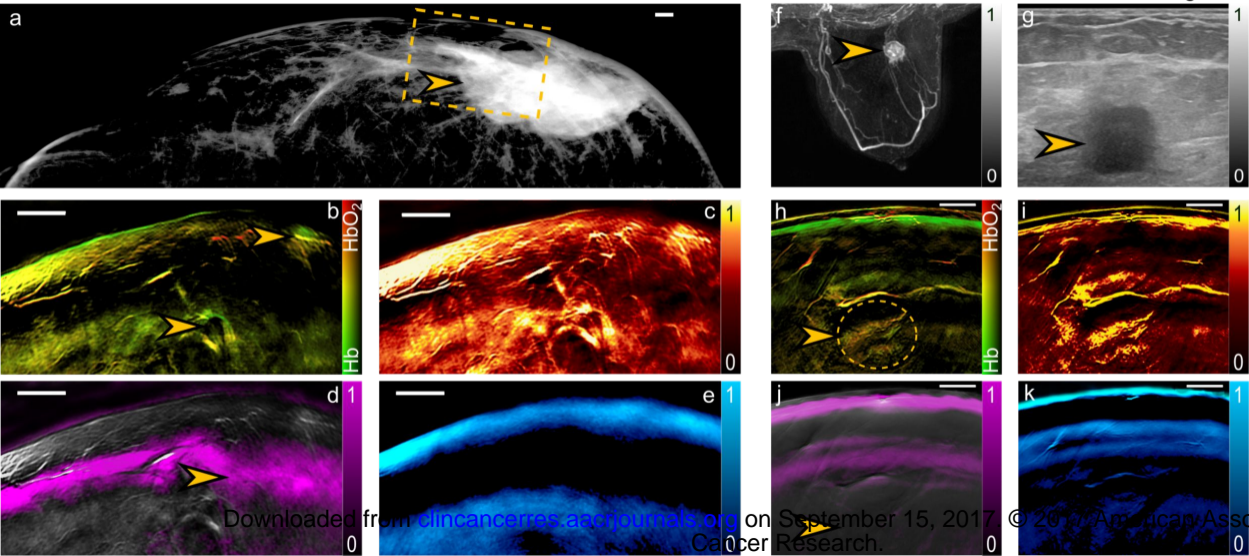
Lipid map

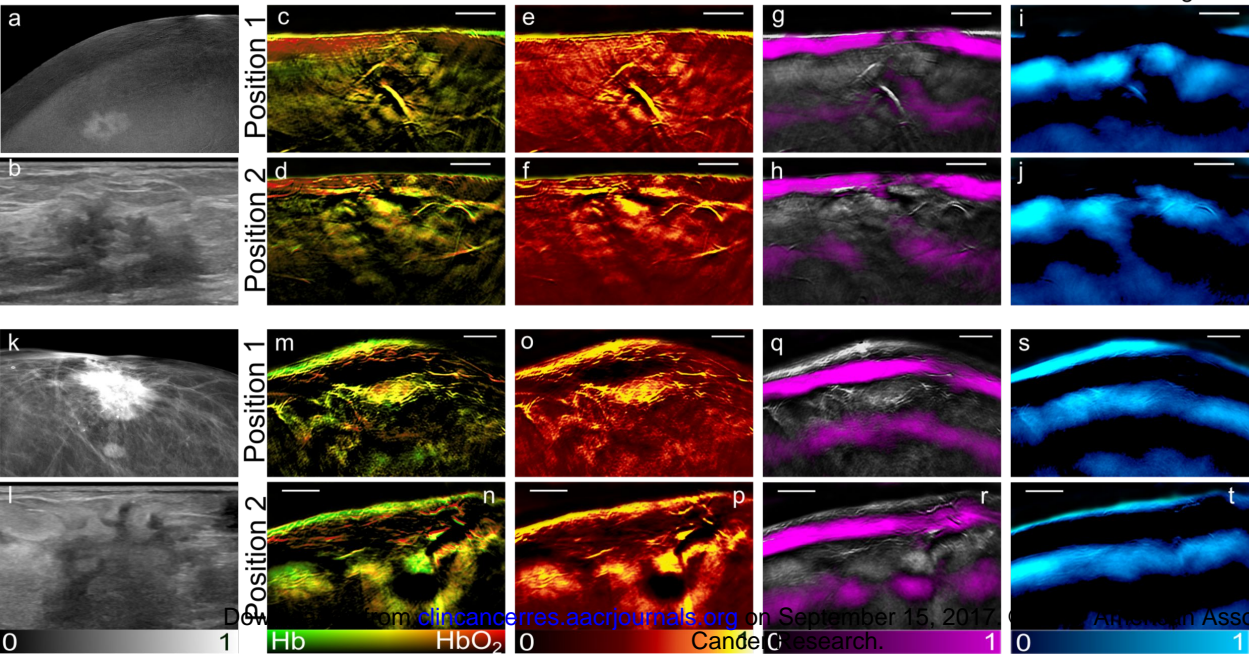


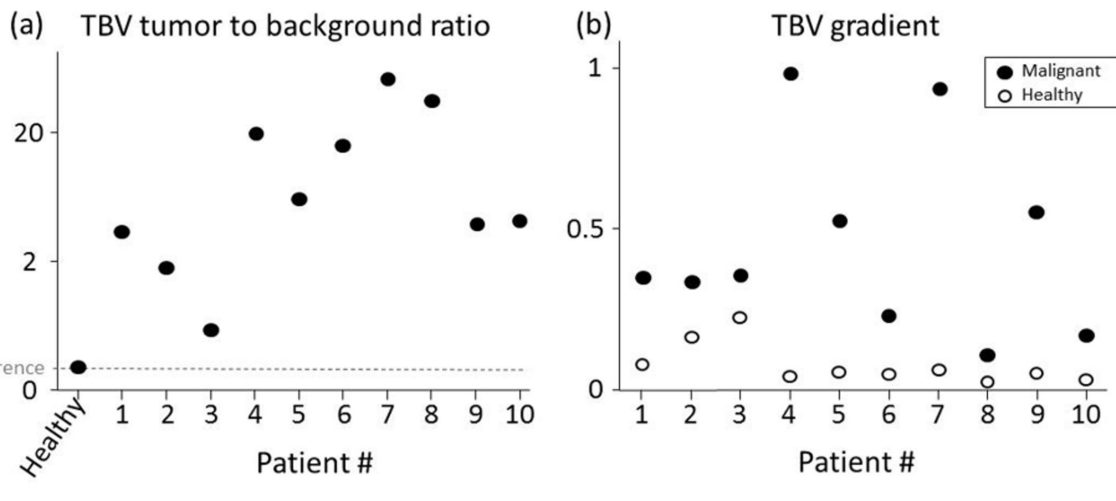
Water map











	Sex	Age	Type	Stage	ER	PR	HER 2
Patient 1	F	74	NST	2	pos	pos	pos
Patient 2	F	64	ILC	2	pos	pos	neg
Patient 3	F	81	NST	2	pos	pos	neg
Patient 4	F	57	NST	3	neg	neg	neg
Patient 5	F	81	NST	2	pos	pos	neg
Patient 6	F	82	NST	2	pos	pos	2+
Patient 7	F	76	NST	2	pos	neg	neg
Patient 8	F	61	NST	2	pos	pos	neg
Patient 9	F	48	ILC	2	pos	pos	neg
Patient 10	M	73	NST	2	pos	pos	2+

Clinical Cancer Research

Multi-Spectral Optoacoustic Tomography (MSOT) of human breast cancer.

Gael Diot, Stephan Metz, Aurelia Noske, et al.

Clin Cancer Res Published OnlineFirst September 12, 2017.

Updated version	Access the most recent version of this article at: doi: 10.1158/1078-0432.CCR-16-3200
Author Manuscript	Author manuscripts have been peer reviewed and accepted for publication but have not yet been edited.

E-mail alerts	Sign up to receive free email-alerts related to this article or journal.
Reprints and Subscriptions	To order reprints of this article or to subscribe to the journal, contact the AACR Publications Department at pubs@aacr.org .
Permissions	To request permission to re-use all or part of this article, contact the AACR Publications Department at permissions@aacr.org .